

Computational Analysis and Optimization of Geometric Parameters for Fibrous Scaffold Design

Rio Parsons, Jesse M. Sestito, and Bethany S. Luke*

Cite This: *ACS Omega* 2022, 7, 41449–41460

Read Online

ACCESS |



Metrics & More

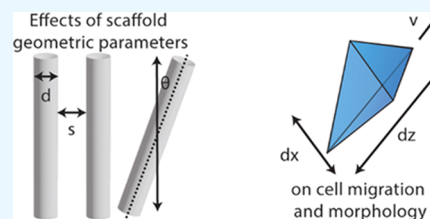


Article Recommendations



Supporting Information

ABSTRACT: Bioresorbable tissue scaffolds are a promising potential treatment for soft-tissue injuries, such as tendon and ligament rupture. These materials provide temporary support to the injured tissues and provide biological cues that promote healing. Previous work has shown that fiber alignment, diameter, and spacing affect cell morphology and migration, which impact healing of the target tissue. However, previous work has not fully characterized the isolated effects of fiber alignment, diameter, and spacing on cell morphology and migration, nor has it revealed the ideal combinations of diameter and spacing to promote cell migration and elongation on fibrous scaffolds. To clarify these effects, a mesoscale model was formulated to describe cell movement on a fibrous scaffold and analyze the isolated effects of fiber alignment, diameter, and spacing. After analyzing the isolated effects, an optimization was performed to find combinations of fiber diameter and spacing that maximized cell elongation and migration, which may lead to improved healing of the target tissue. This analysis may ultimately aid the design of scaffold materials to improve outcomes after tendon or ligament rupture.



1. INTRODUCTION

Biodegradable tissue scaffolds are a promising technology in regenerative medicine.^{1,2} This technology may become a viable treatment option for soft-tissue injuries, such as tendon and ligament rupture, which typically do not fully heal because of the disorganized nature of the newly formed tissue. Disorganized tissue structure may lead to pain and loss of function for patients, reducing quality of life. To obtain a more organized structure and improve healing, cell-seeded fibrous scaffolds can be used to direct tissue formation.^{3–5} The resulting tissue is stronger and may eventually lead to better outcomes and improved quality of life after an injury.

To generate an organized structure and distribute tissue, cells must take on an elongated phenotype and migrate through the scaffold.¹ The elongation promotes a tenogenic cell phenotype that produces aligned collagen fibers to mimic the highly aligned collagen structures in healthy ligament and tendon,^{6–8} and the migration promotes distribution of the new tissue throughout the scaffold. Both elongation and migration can be affected by scaffold geometry, which has been studied extensively *in vitro* and in animal models.^{1,4,9,10} Specifically, cell elongation and migration are affected by fiber diameter, fiber spacing (sometimes described as porosity), and fiber alignment, among other factors.¹

Fiber alignment affects both the elongation and migration of mesenchymal stem cells (MSCs),^{6–8} a common choice of cells for scaffold applications. Aligned scaffold fibers lead the cells to elongate and produce aligned collagen fibers that mimic healthy tissue with adequate strength,¹ while randomly oriented fibers do not allow the cells to elongate, leading to weaker tissue structures.¹¹ Aligned fibers also lead to increased migration of the cells,¹² which is often quantified by measuring

velocity.¹ Cells move with higher velocities on aligned fibers compared to randomly oriented fibers, allowing them to better distribute new tissue on the scaffold structure.

Fiber diameter and fiber spacing appear to affect cell migration within a scaffold,^{1,13–15} but few studies have shown the isolated influences of these two variables. One study showed that cell velocity increased as fiber diameter increased when the effect of fiber spacing was removed by placing cells on individual fibers,¹³ and other studies have shown that cells migrate further into scaffolds when fiber diameter and spacing increase simultaneously.^{16,17} However, some studies have shown a nonmonotonic relationship between fiber diameter and velocity with a peak velocity on fiber diameters of around 400 nm.^{12,18} The studies that showed a nonmonotonic relationship did not explicitly report spacing, so the isolated effects of diameter are difficult to determine from those experiments. Due to the varied findings on the effects of fiber diameter and spacing on cell migration, further work is required to determine the isolated effects of fiber diameter and spacing on cell migration.

Fiber spacing and diameter also appear to affect cell elongation, though the independent effects of diameter and spacing have not been well studied. One study demonstrated that cell elongation decreases with increasing fiber width and

Received: August 15, 2022

Accepted: October 20, 2022

Published: November 2, 2022



constant spacing on a micropatterned substrate.¹⁴ However, other studies show that simultaneously increasing fiber width and spacing may lead to increases in aspect ratio,^{1,15} particularly when nanogrooves are compared to microgrooves.¹⁵ Furthermore, another study showed that fiber diameter had no effect on aspect ratio,¹⁸ though this study did not report the spacing of fibers and the spacing may interact with fiber diameter to affect aspect ratio.¹ The discrepancies between these studies could be due to a lack of information on the isolated effects of fiber spacing and diameter, and further analysis is needed to elucidate the effects of fiber diameter and spacing on cell elongation.

To clarify the effects of fiber alignment, diameter, and spacing on cell elongation and migration, a computational model can be developed. Experimental work has begun to reveal these relationships, but the isolated and combined effects of fiber alignment, diameter, and fiber spacing on cell migration and elongation have not been fully assessed. A computational model can tease apart the isolated effects of individual geometric parameters and may be used to identify optimal combinations of geometric parameters to promote appropriate cell migration and elongation within fibrous scaffolds.

Computational models have been used to assess the properties of scaffolds using traditional mechanical and multiphysics simulations. For example, one study used finite element modeling (FEM) to relate the macroscopic stiffness of a material to the microscopic “cell-effective” stiffness,¹⁹ and another used FEM to quantify the poroelastic characteristics of fibrous scaffolds under cyclic loading.²⁰ The FEM approach was also used to construct a “chemo-bio-mechanical model” that combined scaffold microstructure, mechanical properties, cytokine signaling, and cells to predict outcomes for wound healing.²¹ Other approaches have been used to study scaffolds, such as diffusion-reaction frameworks that model scaffold degradation.²² However, none of these models explicitly included the influences of fiber alignment, diameter, and spacing on cell elongation and migration, which appear to influence scaffold efficacy.¹

Two previous models were developed to assess cell migration on collagen during cancer metastasis, though changes in cell elongation were not included in either model. One of the models used a lattice Monte Carlo (MC) approach to simulate the migration of the cells.²³ The other model used the forces between the cells and the collagen fibers due to ligand binding to compute the velocity of the cell.²⁴ Both models incorporated a variety of mechanical and chemical factors to account for their effects on cell mobility within collagen constructs, though cell elongation was not incorporated.

To include cell elongation in a computational model, the underlying mechanism of elongation must be addressed. Cells elongate due to actin flows within the cell and focal adhesions between the cell and the underlying substrate.²⁵ The focal adhesions bind to the substrate as the cell moves and eventually unbind as the cell continues to migrate.²⁵ Similar molecular binding and migration processes have been modeled using MC approaches.²⁶ For example, the migration of matrix metalloproteinases on collagen has been modeled with MC schemes.^{27,28} Since MC has been used to model cell motion²³ and to model molecular motion, binding, and unbinding,^{26–28} the MC approach appears to be a suitable choice for modeling binding between cell focal adhesions and the scaffold fibers.

The MC approach seems to be a suitable foundation for a computational model to capture the elongation of a cell as it migrates in fibrous scaffolds with varied fiber alignment, diameter, and spacing.

Coupled with a model of cell migration and elongation on fibrous scaffolds, multiobjective optimization can be used to find optimal combinations of fiber diameter and spacing that maximize cell velocity and elongation. Multiobjective optimization has been used to solve complex design optimization problems for implantable scaffolds.^{29–32} Multiobjective optimization is the process of optimizing multiple competing objectives, such as cell velocity and elongation, by varying input parameters, such as scaffold fiber diameter and spacing.³³ Because the objectives are competing, a single solution typically does not maximize all objectives. As such, instead of finding the maximum solution, a subset of the solutions is found composed of nondominated solutions such that, for each solution, the value of one objective cannot be increased without decreasing the value of one of the others. This set of nondominated solutions is known as the Pareto front. Though the Pareto front can eventually be found from random sampling, random sampling can become computationally infeasible for complex models. Guided optimization methods become important in reducing computation time in the discovery of optimal scaffold geometries.

Thus, in this work, a mesoscale model was developed to assess the independent effects of fiber orientation, diameter, and spacing on cell aspect ratio and migration velocity. Overall, the model results appeared to capture experimental results. The model showed reduced cell velocity and aspect ratio on randomly oriented scaffolds compared to aligned scaffolds and increased velocity and aspect ratio on microfibers compared to nanofibers, in agreement with experimental findings. Furthermore, the model showed the independent effect of fiber spacing on cell aspect ratio and velocity for fibrous scaffolds. After verifying that the model captured experimental findings, multiobjective optimization was set up and performed on the model to obtain a set of optimal geometries that maximized cell velocity and elongation. This analysis revealed optimal combinations of fiber diameter and spacing to promote cell migration and elongation in a fibrous scaffold.

2. METHODOLOGY

2.1. Cell–Fiber Model. **2.1.1. Model Overview.** Figure 1 depicts the inputs, basic features, and outputs of the model. The fiber diameter, spacing, and alignment were specified as inputs prior to the start of each simulation (Figure 1A). The simulations consisted of a single cell moving along cylindrical fibers in a cubic simulation box with edges of 75 μm and periodic boundary conditions (Figure 1B). During the simulations, the outputs (cell migration and elongation) were recorded at each time step (Figure 1C).

2.1.2. Coordinate Systems. To assess cell–fiber interactions, coordinate systems were constructed for each fiber, the cell, and the entire scaffold. The scaffold coordinate system, or reference coordinate system, was located at the center of the simulation box, with orthogonal axes parallel to the edges of the simulation box, as depicted in Figure 2 with the subscript *s*. The cell coordinate system was placed at the geometric centroid of the cell, and its orientation is described in the Supporting Information. The cell coordinate system is denoted with a subscript *c* in Figure 2. Each fiber was rotated and translated in the simulation box, resulting in a unique

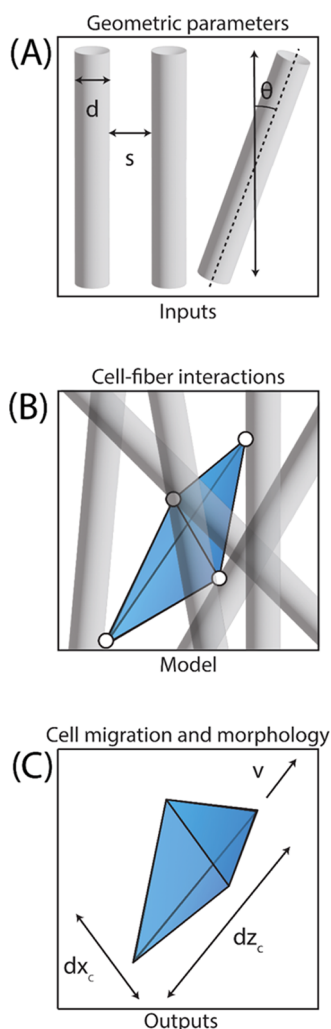


Figure 1. Schematic of input and output parameters for a model of cell–fiber interactions. (A) The geometric parameters serve as the inputs to the model and include fiber diameter (d), fiber spacing (s), and fiber alignment (θ). (B) The model simulates interactions between the cell and the fibers, such as cell adhesion (indicated by white circles) and cell confinement within the scaffold. (C) Cell migration and morphology are outputs of the model. The migration is represented by the velocity of the cell (v), and the elongation of the cell is quantified by the aspect ratio, which can be computed from dx_c and dz_c and the depth of the cell (dy_c , not pictured).

coordinate system for every fiber. An example of a fiber coordinate system is shown in Figure 2, and the construction of the fiber coordinate systems is described in the Supporting Information.

2.1.3. Fiber Geometry. The fibers were constructed by generating discretized points on a cylindrical surface, sequentially rotating those points about their three coordinate axes, and translating the points in space. Each fiber filled a cylindrical volume with five attachment points evenly spaced around its circumference and repeated vertically with a spacing equal to half the circumference of the fiber. Each cylinder had a length equal to the length of the simulation box along the z -axis of the scaffold coordinate frame, resulting in infinitely long fibers when the periodic boundary condition was implemented and the fibers were aligned. Each cylinder was rotated by a random amount about its vertical axis (aligned with the long axis of the fiber) to randomize the positioning of the radial

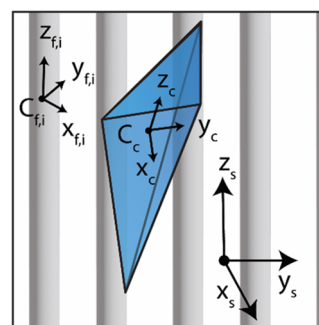


Figure 2. Scaffold (reference) coordinate system, cell coordinate system, and an example of a fiber coordinate system. The scaffold system is denoted with the subscript s , placed at the center of the simulation box, and the axes are parallel to the orthogonal edges of the simulation box. The cell coordinate system is denoted with subscript c , placed at the centroid of the cell, and oriented as described in the Supporting Information. Each fiber has its own coordinate system that is denoted by the subscript f, i , placed at the fiber center, and is oriented as described in the Supporting Information. The fibers and the cell are not to scale in this schematic.

attachment points. For simulations of randomly oriented fibers, the fiber was further rotated by random amounts between zero and π about its other two axes. The Supporting Information contains additional details about the rotations of the fibers. Finally, the rotated fiber was translated along each axis of the scaffold coordinate system such that the centers of the fibers were hexagonally packed with the specified spacing between each fiber. In the aligned state, this arrangement resulted in the hexagonal packing of the fibers in the xy -plane of the scaffold coordinate system. In the randomly oriented state, the centers of the fibers were still hexagonally packed in the xy -plane, but a random vertical translation ensured that the rotation occurred about different points in space, leading to a configuration where any given cross section was not organized into a discernible packing arrangement. The translations are further described in the Supporting Information. After placement of the fibers, the size of the simulation box was adjusted to maintain hexagonal packing and consistent spacing across the periodic boundary.

2.1.4. Cell Representation. The cell was represented as a tetrahedron, whose vertices connected to attachment points on the fibers. At each time step in the simulation, the four cell vertices (or attachment points) attempted to move to a new position coincident with attachment points on the fibers. One of the points on the cell was randomly selected to move first at every time step in a given simulation, while the other three points moved in a random order at each time step, since cells are capable of polarizing and move in a persistent direction.²⁵

2.1.5. Cell–Fiber Interactions. Each time a cell attachment point attempted to move, the algorithm identified all fiber attachment points within a sphere of radius, r_{reach} defined as

$$r_{\text{reach}} = f_{\text{adjust}} * 2.25 \mu\text{m} \quad (1)$$

where 2.25 is the maximum value of r_{reach} in μm and f_{adjust} is an adjustment factor on the interval $[0,1]$ that can reduce the maximum reach of the cell. f_{adjust} is defined as

$$f_{\text{adjust}} = \begin{cases} 0.4*d + 0.52, & d \leq 1.2 \\ 1, & d > 1.2 \end{cases} \quad (2)$$

where d is the fiber diameter and each constant is a scaling factor that linearly reduces the reach of the cell as the fiber diameter decreases.¹³ The spherical search area and the nearby fiber attachment points are depicted in Figure 3A. The maximum search radius of $2.25 \mu\text{m}$ was selected to allow the cell to move between different fibers without excessive computational cost.

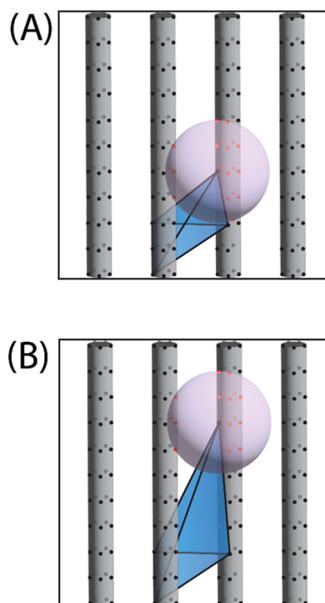


Figure 3. Depiction of nearby attachment points (A) without and (B) with the extension of an attachment point parallel to the direction of the nearest fiber.

Simultaneously, the algorithm shifted the current attachment point along the direction of the current fiber by a distance

$$l_{\text{shift}} = f_{\text{adjust}} * 4.5 \mu\text{m} \quad (3)$$

and identified points within a radius of r_{reach} from the extended point, as depicted in Figure 3B. The maximum shift of $4.5 \mu\text{m}$ was selected to ensure that the points identified in the extended position would not overlap the fiber points identified in the nonextended configuration of the cell described above. The purple spheres in Figure 3 represent the volumes where the top attachment point of the cell can move to a new fiber attachment point. The possible new fiber attachment points are shown in red, and each of them leads to a different cell configuration.

After identifying potential fiber attachment points (shown in red in Figure 3), each possible cell configuration was assessed to determine whether the cell would maintain an acceptable volume. The volume was determined in the cell coordinate system, whose axes aligned with the cell (further described in the Supporting Information), by constructing a box that bounded the cell (Figure 4A) and computing the volume of an ellipsoid with the same dimensions as the bounding box (Figure 4B). The ellipsoid volume (V) was computed using the equation

$$V = \pi * \frac{dx_c}{2} * \frac{dy_c}{2} * \frac{dz_c}{2} \quad (4)$$

where dx_c is the distance between the maximum and minimum x -positions of the cell attachment points, dy_c is the distance

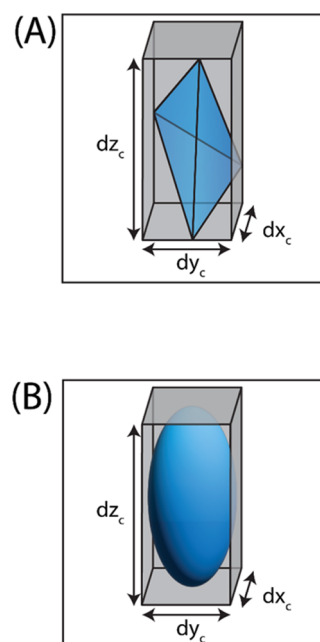


Figure 4. Depiction for cell volume calculation. (A) Cell position was transformed into the cell coordinate system. (B) Dimensions of the bounding box in the cell coordinate frame were used to construct an ellipsoid with the same dimensions and compute the approximate volume of the cell. These dimensions were also used to compute the aspect ratio of the cell.

between the maximum and minimum y -positions, and dz_c is the distance between the maximum and minimum z -positions of the cell in the cell coordinate frame.

The nominal volume of the cell was $4000 \mu\text{m}^3$, and the cell volume was allowed to vary between 50 and 100% of the nominal volume, consistent with experimental observations.³⁴ After determining the volume for each potential configuration of the cell, the configurations with a volume outside of the specified bounds were removed from consideration.

The remaining configurations were assessed to determine whether the cell would fold in on itself. To do so, a plane was constructed from the three points (points A, B, and C in Figure 5A) on the cell tetrahedron other than the moving attachment point. The plane was constructed by defining two vectors originating at point B and pointing toward A and C (Figure 5A), then taking their cross product to generate a vector perpendicular to the plane (vector N in Figure 5A). Next, a vector was constructed from point B to the moving cell attachment point (point D in Figure 5A), and vector BD was dotted with the normal vector

$$BD \cdot N = |BD||N|\cos(\alpha) \quad (5)$$

where α is the angle between vectors BD and N , and $|BD|$ and $|N|$ are the magnitudes of the vectors. If the sign of the dot product was positive, α was less than 90° , indicating that vector BD pointed toward the same side of the plane as the normal vector in the initial configuration (Figure 5A). If the sign was negative, α was greater than 90° , indicating that vector BD pointed toward the opposite side of the plane from the normal vector in the initial configuration. Next, vectors were constructed between point B on the plane and every possible new position for point D, a subset of the red points in Figure 3 that maintained the cell volume. Each new vector was dotted with the normal vector, N , and the sign of the result was

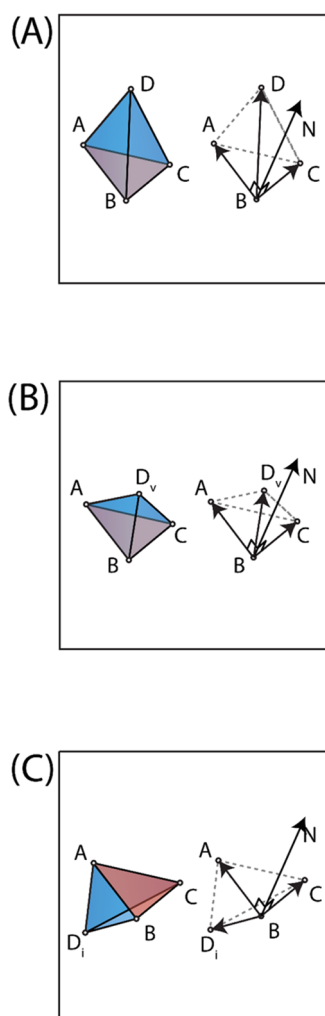


Figure 5. Depiction of vectors used to determine whether or not a cell folds in on itself. (A) Normal vector, N , is constructed by crossing vectors BA and BC . The dot product of N and BD is computed in the initial configuration to determine whether BD points to the same side of plane ABC as N . (B) Example of a valid move for point D . The dot product of BD_v and N would have the same sign as the dot product in the initial configuration. (C) Example of an invalid move for point D . The dot product of BD_i and N would take on the opposite sign of the dot product in the initial configuration.

compared to the sign of $BD \cdot N$ in the initial configuration. If the resulting sign for a potential configuration was the same as the sign of the dot product in the initial configuration, the potential configuration was acceptable because the new vector was on the same side of the plane as the initial configuration. If the resulting sign differed for a potential configuration compared to the initial, the configuration was removed from consideration because it would cause the cell to fold in on itself; point D would move from one side of plane ABC to the opposite side. Figure 5B shows an example of a valid new configuration, and Figure 5C shows an example of an invalid new configuration.

After removing configurations with invalid volumes and configurations where the cell would fold in on itself, the probability of accepting each remaining configuration was determined based on how many fibers the cell would intersect in a new configuration. Figure 6 shows the process used to determine the number of fibers that a cell would intersect in

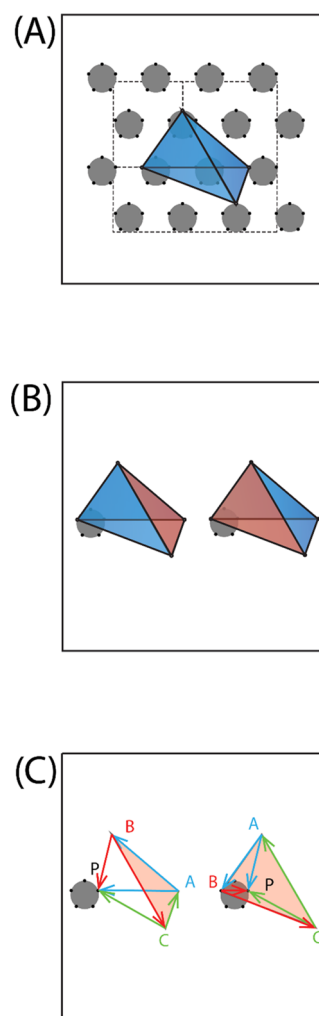


Figure 6. (A) Identification of fibers that the cell might intersect. (B) Depictions of two (red) faces of the tetrahedron used to determine whether the cell intersects a fiber. (C) Depiction of the vectors used to determine whether the faces of the tetrahedron intersect the fiber.

two dimensions. First, the centers of nearby fibers were identified within two fiber radii of the maximum and minimum positions of the cell attachment points along each axis in the scaffold coordinate frame (Figure 6A). Next, the positions of the cell attachment points were transformed (rotated and translated) from the scaffold coordinate frame into the coordinate frame of each fiber identified in the previous step. Once the cell was transformed into a fiber's coordinate system, analysis could be performed in two dimensions (the xy -plane), since the vertical axis of the fiber coordinate system pointed perpendicular to the fiber cross section.

In each of the fiber coordinate frames, cell–fiber intersections were identified by determining whether any faces of the cell tetrahedron encompassed either the fiber center or fiber attachment points in the xy -plane of the fiber coordinate system. To do so, the algorithm isolated the xy -coordinates of the vertices for each face of the cell tetrahedron (two faces are shown in red in Figure 6B) and created vectors around the outer edge of the face (AB , BC , and CA in Figure 6C). Next, the algorithm created vectors from each vertex to a fiber attachment point (AP , BP , and CP in Figure 6C) or the center of the current fiber and then took the cross products of the vectors that originated from the same vertex. In Figure 6,

vector AB would be crossed with vector AP (both shown in blue and originating at point A), vectors BC and BP would be crossed (shown in red), and vectors CA and CP would be crossed (shown in green). The fiber attachment point (point P) is inside the triangular face if the z -components of the three cross products all have the same sign. If the signs of the z -components differ, the point is not inside the triangle. The cross products were repeated for all four triangular faces of the tetrahedron and repeated for all fiber attachment points and the center of the current fiber. If any of the triangular faces encompassed two fiber attachment points or the fiber center, the cell intersected that fiber. This process was repeated for all of the nearby fibers in a potential cell configuration, and the number of cell–fiber intersections was tallied for each possible cell configuration.

The number of intersections was used to determine the probability of accepting a configuration. Every additional intersection reduced the relative probability of accepting a configuration (p_i) by a factor of two, as described by the equations

$$1 = \frac{1}{n} \sum_{i=0}^k n_i * p_i \quad (6)$$

and

$$p_i = 2^{k-i} * p_k \quad (7)$$

where i is the number of fibers intersected in a particular configuration, k is the maximum number of fibers intersected for a group of possible configurations, n is the number of possible cell configurations, n_i is the number of cell configurations where i fibers are intersected, p_i is the relative probability of accepting a configuration with i intersections, and p_k is the probability of accepting a cell configuration with k intersections. Eq 6 was implemented to ensure that the probabilities of all possible configurations sum to one, and eq 7 was implemented to reduce the acceptance probability by a factor of two for every additional fiber that the cell would intersect in a particular configuration. p_k was determined for each set of possible cell configurations by substituting eq 7 into 6 to obtain

$$1 = \frac{1}{n} \sum_{i=0}^k n_i * 2^{k-i} * p_k \quad (8)$$

$$n / \sum_{i=0}^k n_i * 2^{k-i} = p_k \quad (9)$$

The value of p_k could then be used to determine the probabilities of accepting configurations with n_i intersections. Once the probabilities were determined, a particular configuration was randomly selected using those probabilities and a Monte Carlo approach with a uniform random number generator.

2.1.6. Time-Step Calibration. To determine the duration of each simulation step, 12 simulations were run to compute the average displacement (l) of the cell centroid per simulation step with a fiber diameter of 1.2 μm and fiber spacing of 2 μm over 150 simulation steps. The average displacement and a known cell velocity were used to compute the time increment with the formula

$$v = \frac{l}{t} \quad (10)$$

where v is the cell velocity on a single fiber with a diameter of 1.2 μm (experimentally reported)¹³ and t is the duration of each simulation time step. Subsequent analyses were performed using the time step computed from this calibration.

2.1.7. Aspect Ratio Calculation. Aspect ratio was computed using a procedure similar to the one used to compute the volume. The cell position was transformed into the cell coordinate system, a bounding box was constructed around the cell, and the dimensions of the bounding box were used to compute the aspect ratio (AR) using the equation

$$\text{AR} = \frac{\text{length of longest edge}}{\text{average length of other edges}} \quad (11)$$

In Figure 4, the aspect ratio would be

$$\text{AR} = \frac{2 * dz_c}{dx_c + dy_c} \quad (12)$$

2.2. Analysis of Intersection Penalty and Cell Extension Algorithm. Two modeling features were assessed to determine whether they would reduce cell velocity and aspect ratio on randomly oriented scaffolds. The first feature was the statistical penalty for intersecting fibers, and the second feature was the extension of a cell pseudopod along the direction of the nearest fiber. Four combinations of these features were tested: 1) no penalty with no extension, 2) penalty with no extension, 3) no penalty with extension, and 4) penalty with extension. For every combination, six replicate simulations were performed on aligned scaffolds and randomly oriented scaffolds with fiber diameters of 1.2 μm , spacing of 2 μm , and 14 h of simulation time. Student's t tests were used to determine whether scaffold orientation caused a significant reduction in velocity or aspect ratio for each combination of model features with a significance level of 0.05.

2.3. Scaffold Geometry Studies. **2.3.1. Orientation, Diameter, and Spacing Analysis.** To study the effects of fiber orientation on cell velocity and aspect ratio, cell motion was measured on scaffolds with aligned and randomly oriented fibers. The rotation angle (θ) was set to zero in eqs S2 and S4 to obtain aligned fibers and set equal to π to obtain random fiber orientations. In these simulations, fiber spacing was set equal to 2 μm , fiber diameter was set to 1.2 μm , and 24 h of cell motion were simulated. Twelve repetitions of each condition were performed, each with a different random seed.

Fiber diameter was varied to study its effects on cell velocity and aspect ratio over the course of 24 h. The diameter was set to 0.4, 0.7, or 1.2 μm on aligned fibers with a constant spacing of 2 μm . These diameters were chosen to match the diameters in experimental literature.¹³ Twelve repetitions were performed for each diameter with different random seeds, and the means and standard deviations for each diameter were computed.

Cell velocity and aspect ratio were also computed as functions of fiber spacing at a constant diameter of 1.2 μm on aligned fibers after 24 h of simulation time. Fiber spacing, s , as depicted in Figure 7, was set to 1, 1.5, or 2 μm to obtain scaffold volume fractions similar to experimentally reported volume fractions.⁴ The relationship between spacing and volume fraction is derived in the Supporting Information.

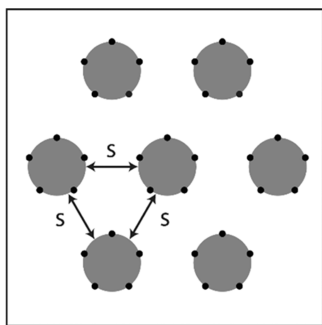


Figure 7. Depiction of fiber spacing (s). The arrows indicate the spacing between fibers, which was defined as the distance between two parallel tangent lines on the circular cross sections of adjacent fibers.

Again, 12 repetitions were performed for each condition, and the means and standard deviations were computed.

2.3.2. Statistics. One-way ANOVA and Tukey–Kramer post hoc testing were used to identify significant differences in cell velocity and aspect ratio due to changes in fiber diameter and fiber spacing. Student's t tests were used to determine whether the fiber alignment resulted in significant differences in velocity and aspect ratio.

2.4. Multiobjective Optimization of Aligned Scaffold Geometry. Once the mesoscale model of cell motion on scaffold fibers was verified, the next task was to explore various scaffold geometries that maximized the cell velocity and elongation. A multiobjective Bayesian optimization approach was used to guide the input parameter selection to search for Pareto solutions. Bayesian optimization works by building a surrogate model from a current set of samples and solutions. This surrogate was used in an acquisition function, which, when maximized, recommended the next sample that was most likely to produce an optimal solution.

In this implementation, a Gaussian process (GP) model with a radial basis function kernel was used as the surrogate. The implementation of the GP model was based on the design and analysis of computer experiment toolkit for MATLAB.³⁵ The acquisition function was based on the expected improvement method (EIM) by Zhan et al.³⁶ Traditionally, the EIM acquisition function is only used in single-objective optimization. For the multiobjective optimization, a GP model was built for each objective, and the acquisition function was the Euclidean distance between the expected improvement values for each objective.³⁷

In the scaffold optimization problem, the goal was to maximize the cell velocity and elongation, which vary based on the scaffold geometry. The input parameters for the scaffold geometry are set as fiber diameter (d) and fiber spacing (s). The objectives (f_1 and f_2) are then defined as

$$f_1(d, s) = 1 / \text{AR} \quad (13)$$

and

$$f_2(d, s) = 1 / v \quad (14)$$

and the optimization problem is formulated as

$$\min_{d, s} \{f_1(d, s), f_2(d, s)\} \quad (15)$$

where d and s are bounded by 0.4 and 1.2 μm and 1 and 2 μm , respectively, to be consistent with experimental reports as described above.^{4,13}

Each solution was computed by first creating six scaffolds with the desired input parameters. Then, the cell motion simulation was executed one time for each scaffold. The main controller code and each cell motion simulation were run on their own processor core.³⁸ From the cell motion simulations, the aspect ratio and velocity were extracted and averaged across all simulations. Five initial samples spanning the design space were selected using the Latin hypercube sampling method.^{39,40} These five samples were then passed through the simulation to calculate their corresponding solutions. The algorithm then recommended the next sample, executed the simulation to calculate the corresponding solution, and then repeated it for a total of 105 solutions. This process is outlined in Figure 8.

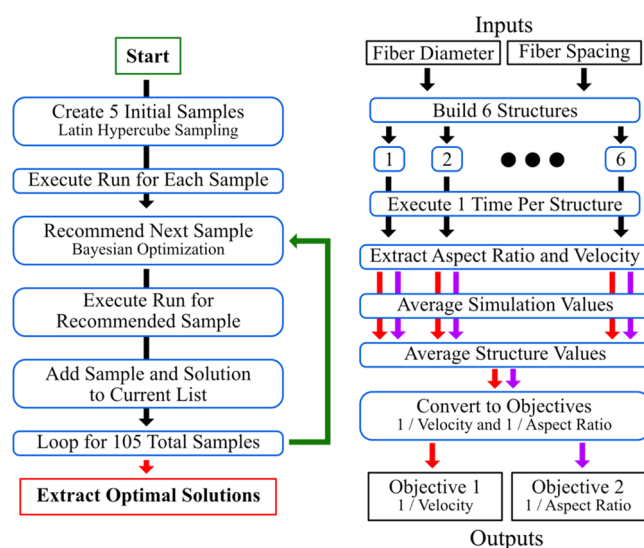


Figure 8. Flowchart of the optimization algorithm used to target optimal structure geometries (left). Flowchart of the simulation run algorithm illustrating the inputs and outputs for each run (right).

3. RESULTS

3.1. Time-Step Calibration. The calibration simulations resulted in an average displacement of 1.042 μm per simulation time step. This displacement and the average experimental velocity of 38 μm per hour¹³ resulted in a duration of 0.027 h per simulation step.

3.2. Analysis of Intersection Penalty and Cell Extension Algorithm. The velocities on the random scaffolds were significantly lower than the aligned scaffolds in the conditions where the extension was implemented (Table 1). The aspect ratios on the random scaffolds were significantly reduced compared to the aligned scaffolds in the conditions where the penalty was implemented (Table 1).

3.3. Scaffold Geometry Studies. Scaffold geometric parameters had significant effects on cell velocity and aspect ratio. Velocity and aspect ratio were significantly reduced on random scaffolds compared to aligned scaffolds (Figure 9). Velocity and aspect ratio were significantly increased on fibers with diameters of 1.2 μm compared to fiber diameters of 0.4 and 0.7 μm (Figure 10). Aspect ratio was not significantly

Table 1. Effect of Scaffold Organization on Cell Velocity and Aspect Ratio with Different Model Features

condition	velocity ($\mu\text{m}/\text{h}$) aligned	velocity ($\mu\text{m}/\text{h}$) random	aspect ratio aligned	aspect ratio random
no penalty, no extension	28.5 \pm 0.7	29.9 \pm 1.1	3.06 \pm 0.96	3.06 \pm 0.54
penalty, no extension	28.5 \pm 0.7	27.7 \pm 0.7	6.02 \pm 1.88	2.16 \pm 0.25*
no penalty, extension	69.3 \pm 8.8	32.8 \pm 5.8*	6.52 \pm 4.50	6.21 \pm 2.83
penalty, extension	81.4 \pm 2.6	25.9 \pm 4.4*	7.50 \pm 2.95	2.95 \pm 0.58*

*Indicates a significant reduction ($p < 0.05$) compared to aligned condition.

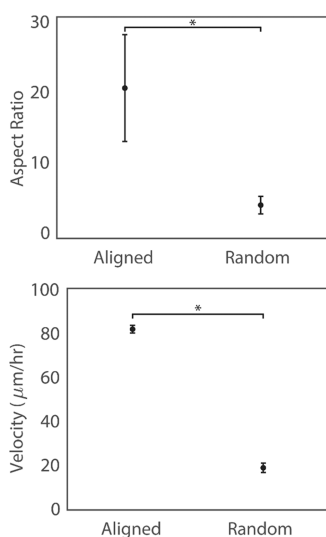


Figure 9. Effect of fiber alignment on cell aspect ratio and velocity. Both aspect ratio and velocity are significantly reduced on randomly oriented scaffolds compared to aligned scaffolds. * indicates $p < 0.05$ using an unpaired Student's t test.

affected by fiber spacing, but velocity significantly decreased as fiber spacing increased (Figure 11).

3.4. Optimization. The optimization algorithm took 24 days to obtain 105 solutions, including the initial 5 solutions, with an average time for each model simulation run of approximately 4.5 h. The resultant solutions are presented in Figure 12. The Pareto solutions are organized by rank.⁴¹ Not including the initial sampling, the current approximated Pareto front took 68 samples to find, and the rank 2 solutions took 94 samples to find. A subset of the samples and solutions are presented in Table 2.

4. DISCUSSION

4.1. Analysis of Intersection Penalty and Cell Extension Algorithm. The results indicate that the model can capture the effects of scaffold orientation on cell velocity and aspect ratio by implementing a statistical penalty and an algorithm to mimic pseudopod extension along fibers. The effect of orientation on aspect ratio can be captured by a penalty alone, and the effect of orientation on velocity can be captured by implementing the extension algorithm alone. However, to capture both effects, both features must be implemented.

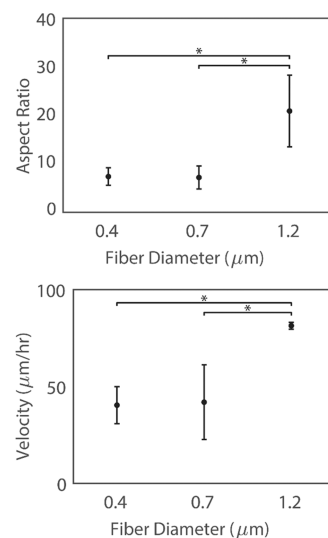


Figure 10. Effect of fiber diameter on cell aspect ratio and velocity. Velocity and aspect ratio increase significantly at a diameter of 1.2 μm compared to diameters of 0.4 and 0.7 μm . * indicates $p < 0.05$ using ANOVA and the Tukey–Kramer post hoc correction.

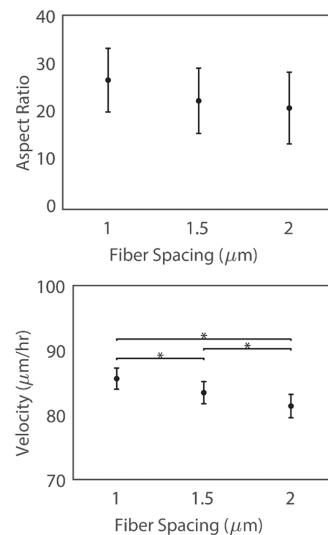


Figure 11. Effect of fiber spacing on cell aspect ratio and velocity. Aspect ratio did not significantly change as a function of fiber spacing. Velocity significantly decreased as fiber spacing increased. * indicates $p < 0.05$ using ANOVA and the Tukey–Kramer post hoc correction.

Previous studies have demonstrated that cells extend a pseudopod, and actin flows cause the rest of the cell to follow when they take on a mesenchymal phenotype.²⁵ Additionally, previous work has demonstrated that cells take on a mesenchymal phenotype when they are unconfined, leading to an increase in velocity and persistence.²⁵ These results appear to be consistent with the findings of this analysis. The model results show a significant increase in velocity on aligned scaffolds (low confinement) when the extension is implemented (mimicking a mesenchymal phenotype) and show no increase in velocity on random scaffolds (higher confinement, leading to more of an amoeboid phenotype; Table 1). The extension appears to allow the cell to move faster on aligned fibers by extending a pseudopod further along the direction of the nearest fiber at each time step.

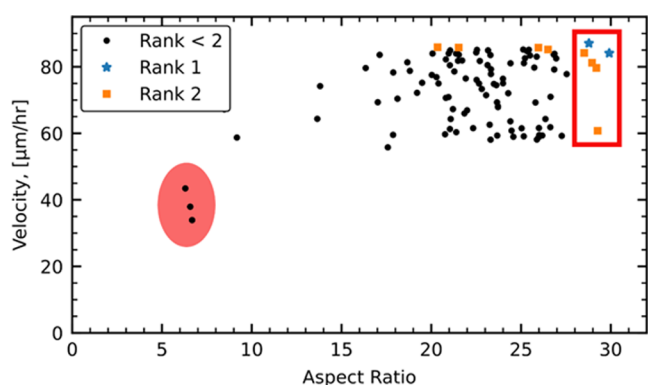


Figure 12. This plot is composed of all 105 solutions from the multiobjective Bayesian optimization algorithm. In general, as the fiber diameter increased and the fiber spacing decreased, the aspect ratio and velocity increased. However, in the red square, decreasing the fiber diameter and increasing the fiber spacing increased the aspect ratio. The red circle highlights the lowest rank solutions, which had scaffold geometric parameters close to a $0.4 \mu\text{m}$ fiber diameter and $2 \mu\text{m}$ fiber spacing, which is the minimum and maximum fiber diameter and fiber spacing allowed per the optimization parameters.

Table 2. Subset of the 105 Samples and Their Corresponding Solutions for the First Two Ranks and the Last Rank

rank	fiber diameter (μm)	fiber spacing (μm)	aspect ratio	velocity ($\mu\text{m}/\text{h}$)
1	1.1997	1.0003	28.78	87.05
1	1.2000	1.1490	29.91	84.09
2	1.0167	1.0269	29.20	79.66
2	1.2000	1.0045	25.97	85.73
2	1.1983	1.0026	21.52	85.79
2	1.1977	1.0002	28.52	84.16
2	1.0920	1.0007	28.96	81.19
2	1.1998	1.1551	20.35	85.86
2	1.1965	1.0027	26.51	85.21
2	0.4801	1.0005	29.27	60.75
⋮				
19	0.4000	2.0000	6.57	37.94
19	0.6869	2.0000	6.30	43.44
19	0.5153	1.9763	6.68	33.91

At volume fractions reported for aligned scaffolds,⁴ cells cannot fit between fibers and maintain a physiological volume⁴² without deforming themselves, the surrounding fibers, or both. To move through the scaffold, the cell must do work to deform itself and/or the scaffold. The work to deform the cell and/or the scaffold could be modeled using finite element modeling (FEM), similar to a previous report.²⁰ However, such an approach would greatly increase the computational costs of simulating cell motion on scaffolds. Instead of using a costly FEM approach, a statistical penalty was used to represent the physical cost of deformation without adding the computational cost required to model hyperelastic materials and/or internal cellular processes that regulate cell deformation.

The penalty in the model appears to cause an increase in aspect ratio on aligned fibers compared to random fibers (Table 1), suggesting that it creates a “preference” for cells to “move” fewer fibers and spend less energy. The elongated configuration allows the cell to intersect fewer fibers on aligned scaffolds, since the cell can extend along a few fibers without

intersecting additional fibers. On random scaffolds, the penalty does not produce elongated cells because elongation along one or a few fibers does not consistently reduce the number of fibers that a cell intersects.

4.2. Scaffold Geometry Studies. Effects of scaffold orientation on aspect ratio and velocity have been well documented. Experiments show that random fiber orientation leads to reduced cell velocity and aspect ratio.^{1,18} The results here capture these trends, showing a significant reduction in both quantities on the randomly oriented scaffolds compared to the aligned scaffolds.

Numerous experiments have demonstrated that fiber diameter influences cell velocity, and the results of this study appear to agree with experimental evidence. Cell velocity increased with diameter in an experiment with cells suspended on single fibers,¹³ consistent with the results of the present study. Cells penetrated further into scaffolds when fiber diameter and porosity were simultaneously increased in two other studies.^{16,17} In other experiments, cell velocity varied nonmonotonically with fiber diameter¹⁸ or decreased with fiber diameter.⁴³ However, in all but one of those studies,¹³ fiber spacing was either covaried with diameter or not reported, making the individual effects of fiber diameter difficult to assess from the experimental evidence alone.

Fiber diameter also appeared to influence the aspect ratio of cells in experiments and the simulations in the present study. In two studies, cells appeared to elongate more on microfibers compared to nanofibers,^{14,15} consistent with the findings in this work. One of these studies also found that aspect ratio decreases on fibers with widths of $15 \mu\text{m}$ compared to fibers with widths of $2 \mu\text{m}$.¹⁴ However, the present study did not assess fiber diameters of $15 \mu\text{m}$, and the model was not easily modifiable to study larger diameters, so additional work would be needed to determine whether the model captures this nonmonotonic change in aspect ratio with fiber size. In another study, aspect ratio was not significantly changed by fiber diameter,¹⁸ though the study did not report the spacing or porosity of the scaffolds. The effects of fiber diameter and spacing have not been addressed separately in most experimental studies, so their effects on aspect ratio are not entirely clear from experiments alone, and the present work may help clarify the isolated effects.

The maximum aspect ratios in this study are higher than aspect ratios reported in previous works,¹⁸ though analysis suggests that the maximum cell lengths are not unreasonably large compared to experimentally reported cell lengths.¹³ Analysis of the simulated cell lengths is described in the Supporting Information and suggests that cells may reach maximal lengths between 102 and $129 \mu\text{m}$ at the maximum aspect ratios reached during the optimization procedure. Experimental measurements have shown cell lengths around $90 \mu\text{m}$,¹³ so the simulated lengths appear to be in reasonably close to published measurements.

The effects of fiber spacing have not been isolated in previous works. Some studies have reported the volume fraction of scaffolds without systematically varying it,⁴ others have covaried spacing with fiber diameter,^{15–17} and others have not included measures of fiber spacing or porosity.^{18,43} The present study found that aspect ratio was not significantly influenced by fiber spacing alone and that velocity significantly decreased as fiber spacing increased at a constant fiber diameter. This result suggests that fiber spacing should be

quantified and controlled in experimental studies to prevent a confounding influence on cell velocity.

While the results of the model appear to be consistent with available experimental data, further experimental work will be required to fully validate the model results. This experimental work would include fabricating scaffolds with the geometric parameters described in this study, seeding the scaffolds with cells, and measuring the velocity and aspect ratio of the cells on the scaffolds using existing techniques. Scaffolds could be fabricated using electrospinning or other techniques described previously.¹ The geometric parameters of the scaffolds could be varied systematically to mimic the conditions tested with the model in this work. These parameters could be controlled by varying the inputs to the electrospinning device, and the resulting scaffolds could be characterized using SEM imaging, as described previously.^{4,18,43} Following fabrication, cells could be seeded onto the scaffolds to allow them to migrate and elongate. To quantify migration and elongation, bright field and fluorescence microscopy could be used for time-lapse images of the positions and morphologies of the cells.^{18,43} The results of these studies could be used to further validate and refine the model presented in this work.

4.3. Optimization. The optimization algorithm was set up to target solutions that maximized velocity and aspect ratio. Most of the solutions had high values for velocity and aspect ratio, and only a few solutions had low values for velocity and aspect ratio, as demonstrated in Figure 12 by the drastic difference between the lowest three samples (circled in red) and the rest of the samples. These results suggest that the algorithm successfully targeted expected optimums that maximized velocity and aspect ratio. In general, the expected optimums were found by increasing fiber diameter and decreasing fiber spacing, consistent with the results of the isolated analyses of diameter and spacing. However, three of the optimums (Pareto solutions) were found by slightly decreasing diameter and slightly increasing spacing, which was counterintuitive based on the overall pattern.

Though a systematic sweep of the inputs could be used to locate optimal solutions, this approach would be computationally challenging due to the model execution time. A systematic sweep becomes even more computationally challenging as the model is improved over time and the number of input variables increases. Additionally, small details can be missed through a systematic sweep. For example, a systematic sweep might miss the slight increase in aspect ratio that occurs when diameter decreases and spacing increases. Instead, by targeting optimums using optimization, the total number of simulations necessary to discover the Pareto front decreases. Overall, the optimization algorithm appears to successfully target optimal solutions with a methodology that can be expanded as the model develops.

As the model evolves to include more than two input parameters for optimization, this optimization setup can be expanded to capture the increasing design space. However, to keep optimization computation time low as model computation time increases, the optimization approach may need to be improved. To do so, the optimization approach could incorporate better initial sampling, an acquisition function that balances exploration and exploitation⁴⁴ and batch optimization. By improving the initial sampling and balancing exploration and exploitation, the number of samples required to find the Pareto front could be reduced. Batch optimization is done by parallelizing the algorithm to suggest multiple

samples at a time and computing their corresponding solutions in parallel. This method increases the computation time but reduces optimization time, which can be valuable when the computation time to calculate a single solution is high (as in the present model), but the computational resources are inexpensive.

4.4. Model Applications. This model could be used to improve scaffold design by identifying scaffold geometric parameters that promote cell migration and elongation. Cell elongation is critical to scaffold success in ligaments and tendons because elongation leads to a tenogenic phenotype that produces aligned collagen fibers that restore the structure of the damaged tissue.^{6–8} Cell migration is critical to scaffold success because it allows the tissue to be distributed throughout a scaffold. While many studies have noted that migration and elongation are affected by the diameter, spacing, and alignment of the fibers within a scaffold,¹ the combined influences of these parameters have not been assessed systematically with experiments. In this study, the combined influences of diameter and spacing were assessed and revealed that migration and elongation are maximized when fibers are closely packed, and their diameters are larger. These geometric parameters could be used in the design of scaffolds to maximize cell elongation and migration, which would promote aligned tissue formation and distribution of tissue that would restore the native structures of ligaments and tendons.

While this model was designed to study cell motion on fibrous scaffolds, it could also be adapted to study other biological phenomena where cells interact with fibrous materials. For example, the model could be adapted to study cell migration and elongation in healthy or damaged ligaments and tendons, since ligaments and tendons have similar structures to fibrous scaffolds.^{1,4,9} The model could also be adapted to study how the organization of extracellular matrix affects cell migration during cancer metastasis, similar to a previous model.²³ Indeed, the model could be adapted to study the interactions between tissues and cells throughout the body due to the similarities in fiber structure.

4.5. Limitations. The model presented in this work relies on simplifications to both cell behavior and scaffold properties. These simplifications helped isolate geometric effects but prevented the model from being used to study how scaffold mechanics affect the cell, how the internal cellular machinery affects cell motion, or how chemical and biological factors affect cell morphology and motion. However, previous studies have addressed the mechanical properties of scaffolds,^{13,19,20} others have studied cellular responses to scaffold materials,^{1,5–8,12–18,42} and numerous studies have assessed the effects of biological and chemical signaling.^{1,11} While these studies provide critical insights, previous work has not isolated the effects of scaffold geometry. This work serves as a starting point to address isolated effects of geometry on cell morphology and migration and may be combined with other approaches to gain further insights into the complex interactions between cells and scaffolds.

5. CONCLUSIONS

In this work, a mesoscale model was developed to assess the independent effects of fiber orientation, diameter, and spacing on cell aspect ratio and migration velocity. Overall, the model results appeared to capture experimental results and revealed the independent effects of fiber spacing (porosity) on cell aspect ratio and velocity, which have not been clearly reported

previously. Additionally, a scalable multiobjective Bayesian optimization schema was created and executed to perform scaffold design optimization that maximizes cell aspect ratio and velocity. This analysis may help reveal geometric scaffold parameters that would promote a balance between cell migration and elongation, guide design for experimental production of ligament and tendon scaffolds, and, ultimately, provide a better treatment option for patients with ligament and tendon injuries.

■ ASSOCIATED CONTENT

SI Supporting Information

The Supporting Information is available free of charge at <https://pubs.acs.org/doi/10.1021/acsomega.2c05234>.

Additional methodological details including derivations of the cell coordinate system, the rotation matrices for fibers, the relationship between volume fraction and fiber spacing, and the relationships between aspect ratio, volume, and cell length (PDF)

■ AUTHOR INFORMATION

Corresponding Author

Bethany S. Luke – Department of Mechanical Engineering and Bioengineering, Valparaiso University, Valparaiso, Indiana 46383, United States; orcid.org/0000-0003-4184-7294; Email: Bethany.Luke@valpo.edu

Authors

Rio Parsons – Department of Mechanical Engineering and Bioengineering, Valparaiso University, Valparaiso, Indiana 46383, United States

Jesse M. Sestito – Department of Mechanical Engineering and Bioengineering, Valparaiso University, Valparaiso, Indiana 46383, United States; orcid.org/0000-0002-4489-7054

Complete contact information is available at:

<https://pubs.acs.org/doi/10.1021/acsomega.2c05234>

Notes

The authors declare no competing financial interest.

■ ACKNOWLEDGMENTS

The authors would like to thank Dr. Nicholas Rosasco for allowing them to use the Valparaiso University Compute Resources to run simulations and the optimization. The authors would also like to thank Dr. Reva Johnson for her assistance with manuscript preparation. This work was not externally funded. The authors are grateful to the Department of Mechanical Engineering and Bioengineering at Valparaiso University for their support of this work.

■ REFERENCES

- (1) Jenkins, T. L.; Little, D. Synthetic Scaffolds for Musculoskeletal Tissue Engineering: Cellular Responses to Fiber Parameters. *npj Regen. Med.* **2019**, *4*, 15.
- (2) Ruan, D.; Zhu, T.; Huang, J.; Le, H.; Hu, Y.; Zheng, Z.; Tang, C.; Chen, Y.; Ran, J.; Chen, X.; Yin, Z.; Qian, S.; Pioletti, D.; Heng, B. C.; Chen, W.; Shen, W.; Ouyang, H. W. Knitted Silk-Collagen Scaffold Incorporated with Ligament Stem/Progenitor Cells Sheet for Anterior Cruciate Ligament Reconstruction and Osteoarthritis Prevention. *ACS Biomater. Sci. Eng.* **2019**, *5*, 5412–5421.
- (3) Liu, H.; Yang, L.; Zhang, E.; Zhang, R.; Cai, D.; Zhu, S.; Ran, J.; Bunpetch, V.; Cai, Y.; Heng, B. C.; Hu, Y.; Dai, X.; Chen, X.; Ouyang, H. Biomimetic Tendon Extracellular Matrix Composite Gradient

Scaffold Enhances Ligament-to-Bone Junction Reconstruction. *Acta Biomater.* **2017**, *56*, 129–140.

(4) Sensini, A.; Gualandi, C.; Focarete, M. L.; Belcari, J.; Zucchelli, A.; Boyle, L.; Reilly, G. C.; Kao, A. P.; Tozzi, G.; Cristofolini, L. Multiscale Hierarchical Bioresorbable Scaffolds for the Regeneration of Tendons and Ligaments. *Biofabrication* **2019**, *11*, 035026.

(5) Younesi, M.; Islam, A.; Kishore, V.; Anderson, J. M.; Akkus, O. Tenogenic Induction of Human MSCs by Anisotropically Aligned Collagen Biotextiles. *Adv. Funct. Mater.* **2014**, *24*, 5762–5770.

(6) Trappmann, B.; Gautrot, J. E.; Connelly, J. T.; Strange, D. G. T.; Li, Y.; Oyen, M. L.; Cohen Stuart, M. A.; Boehm, H.; Li, B.; Vogel, V.; Spatz, J. P.; Watt, F. M.; Huck, W. T. S. Extracellular-Matrix Tethering Regulates Stem-Cell Fate. *Nat. Mater.* **2012**, *11*, 642–649.

(7) Zhang, C.; Yuan, H.; Liu, H.; Chen, X.; Lu, P.; Zhu, T.; Yang, L.; Yin, Z.; Heng, B. C.; Zhang, Y.; Ouyang, H. Well-Aligned Chitosan-Based Ultrafine Fibers Committed Teno-Lineage Differentiation of Human Induced Pluripotent Stem Cells for Achilles Tendon Regeneration. *Biomaterials* **2015**, *53*, 716–730.

(8) Yin, Z.; Chen, X.; Chen, J. L.; Shen, W. L.; Hieu Nguyen, T. M.; Gao, L.; Ouyang, H. W. The Regulation of Tendon Stem Cell Differentiation by the Alignment of Nanofibers. *Biomaterials* **2010**, *31*, 2163–2175.

(9) Freedman, B. R.; Mooney, D. J. Biomaterials to Mimic and Heal Connective Tissues. *Adv. Mater.* **2019**, *31*, 1806695.

(10) Liu, W.; Lipner, J.; Xie, J.; Manning, C. N.; Thomopoulos, S.; Xia, Y. Nanofiber Scaffolds with Gradients in Mineral Content for Spatial Control of Osteogenesis. *ACS Appl. Mater. Interfaces* **2014**, *6*, 2842–2849.

(11) Shiroud Heidari, B.; Ruan, R.; De-Juan-Pardo, E. M.; Zheng, M.; Doyle, B. Biofabrication and Signaling Strategies for Tendon/Ligament Interfacial Tissue Engineering. *ACS Biomater. Sci. Eng.* **2021**, *7*, 383–399.

(12) Qu, J.; Zhou, D.; Xu, X.; Zhang, F.; He, L.; Ye, R.; Zhu, Z.; Zuo, B.; Zhang, H. Optimization of Electrospun TSF Nanofiber Alignment and Diameter to Promote Growth and Migration of Mesenchymal Stem Cells. *Appl. Surf. Sci.* **2012**, *261*, 320–326.

(13) Meehan, S.; Nain, A. S. Role of Suspended Fiber Structural Stiffness and Curvature on Single-Cell Migration, Nucleus Shape, and Focal-Adhesion-Cluster Length. *Biophys. J.* **2014**, *107*, 2604–2611.

(14) Abagnale, G.; Steger, M.; Nguyen, V. H.; Hersch, N.; Sechi, A.; Jousen, S.; Denecke, B.; Merkel, R.; Hoffmann, B.; Dreser, A.; Schnakenberg, U.; Gillner, A.; Wagner, W. Surface Topography Enhances Differentiation of Mesenchymal Stem Cells towards Osteogenic and Adipogenic Lineages. *Biomaterials* **2015**, *61*, 316–326.

(15) Watari, S.; Hayashi, K.; Wood, J. A.; Russell, P.; Nealey, P. F.; Murphy, C. J.; Genetos, D. C. Modulation of Osteogenic Differentiation in HMSCs Cells by Submicron Topographically-Patterned Ridges and Grooves. *Biomaterials* **2012**, *33*, 128–136.

(16) Powell, H. M.; Boyce, S. T. Fiber Density of Electrospun Gelatin Scaffolds Regulates Morphogenesis of Dermal-Epidermal Skin Substitutes. *J. Biomed. Mater. Res.* **2008**, *84A*, 1078–1086.

(17) Sisson, K.; Zhang, C.; Farach-Carson, M. C.; Chase, D. B.; Rabolt, J. F. Fiber Diameters Control Osteoblastic Cell Migration and Differentiation in Electrospun Gelatin. *J. Biomed. Mater. Res.* **2010**, *94*, 1312–1320.

(18) Kievit, F. M.; Cooper, A.; Jana, S.; Leung, M.; Wang, K.; Edmondson, D.; Wood, D.; Lee, J.; et al. Aligned Chitosan-Polycaprolactone Polyblend Nanofibers Promote the Migration of Glioblastoma Cells. *Adv. Healthcare Mater.* **2013**, *2*, 1651.

(19) Herrera, A.; Hellwig, J.; Leemhuis, H.; von Klitzing, R.; Heschel, I.; Duda, G. N.; Petersen, A. From Macroscopic Mechanics to Cell-Effective Stiffness within Highly Aligned Macroporous Collagen Scaffolds. *Mater. Sci. Eng.: C* **2019**, *103*, 109760.

(20) Yerrabelli, R. S.; Somers, S. M.; Grayson, W. L.; Spector, A. A. Modeling the Mechanics of Fibrous-Porous Scaffolds for Skeletal Muscle Regeneration. *Med. Biol. Eng. Comput.* **2021**, *59*, 131–142.

(21) Sohutskey, D. O.; Buganza Tepole, A.; Voytk-Harbin, S. L. Mechanobiological Wound Model for Improved Design and

Evaluation of Collagen Dermal Replacement Scaffolds. *Acta Biomater.* **2021**, *135*, 368–382.

(22) Chen, Y.; Zhou, S.; Li, Q. Mathematical Modeling of Degradation for Bulk-Erosive Polymers: Applications in Tissue Engineering Scaffolds and Drug Delivery Systems. *Acta Biomater.* **2011**, *7*, 1140–1149.

(23) Harjanto, D.; Zaman, M. H. Modeling Extracellular Matrix Reorganization in 3D Environments. *PLoS One* **2013**, *8*, e52509.

(24) Harjanto, D.; Zaman, M. H. Computational Study of Proteolysis-Driven Single Cell Migration in a Three-Dimensional Matrix. *Ann. Biomed. Eng.* **2010**, *38*, 1815–1825.

(25) Callan-Jones, A. C.; Voituriez, R. Actin Flows in Cell Migration: From Locomotion and Polarity to Trajectories. *Curr. Opin. Cell Biol.* **2016**, *38*, 12–17.

(26) *Biomaterials and Materials for Medicine*, Li, J., Ed.; CRC Press: Boca Raton, FL, 2022.

(27) Sarkar, S. K.; Marmer, B.; Goldberg, G.; Neuman, K. C. Single-Molecule Tracking of Collagenase on Native Type I Collagen Fibrils Reveals Degradation Mechanism. *Curr. Biol.* **2012**, *22*, 1047–1056.

(28) Powell, B.; Malaspina, D. C.; Szeleifer, I.; Dhaher, Y. Effect of Collagenase–Gelatinase Ratio on the Mechanical Properties of a Collagen Fibril: A Combined Monte Carlo–Molecular Dynamics Study. *Biomech. Model. Mechanobiol.* **2019**, *18*, 1809–1819.

(29) Boccaccio, A.; Uva, A. E.; Fiorentino, M.; Mori, G.; Monno, G. Geometry Design Optimization of Functionally Graded Scaffolds for Bone Tissue Engineering: A Mechanobiological Approach. *PLoS One* **2016**, *11*, e0146935.

(30) Reina-Romo, E.; Papantoniou, I.; Bloemen, V.; Geris, L. Computational Design of Tissue Engineering Scaffolds. In *Handbook of Tissue Engineering Scaffolds: Volume One*, Elsevier, 2019; pp 73–92.

(31) Arabnejad Khanoki, S.; Pasini, D. Multiscale Design and Multiobjective Optimization of Orthopedic Hip Implants with Functionally Graded Cellular Material. *J. Biomech. Eng.* **2012**, *134*, 780.

(32) Bidan, C. M.; Kommareddy, K. P.; Rumpfer, M.; Kollmannsberger, P.; Fratzl, P.; Dunlop, J. W. C. Geometry as a Factor for Tissue Growth: Towards Shape Optimization of Tissue Engineering Scaffolds. *Adv. Healthcare Mater.* **2013**, *2*, 186–194.

(33) *Theory of Multiobjective Optimization*, Sawaragi, Y.; Nakayama, H.; Tanino, T., Eds.; Elsevier Science, 1985.

(34) Guo, M.; Pegoraro, A. F.; Mao, A.; Zhou, E. H.; Arany, P. R.; Han, Y.; Burnette, D. T.; Jensen, M. H.; Kasza, K. E.; Moore, J. R.; Mackintosh, F. C.; Fredberg, J. J.; Mooney, D. J.; Lippincott-Schwartz, J.; Weitz, D. A. Cell Volume Change through Water Efflux Impacts Cell Stiffness and Stem Cell Fate. *Proc. Natl. Acad. Sci. U.S.A.* **2017**, *114*, E8618–E8627.

(35) Lophaven, S.; Nielsen, H.; Søndergaard, J. *DACE - A MATLAB Kriging Toolbox Version 2.0, Technical Report IMM-TR-2002-12*, 2002.

(36) Zhan, D.; Cheng, Y.; Liu, J. Expected Improvement Matrix-Based Infill Criteria for Expensive Multiobjective Optimization. *IEEE Trans. Evol. Comput.* **2017**, *21*, 956–975.

(37) Sestito, J. M.; Thatcher, M. L.; Shu, L.; Harris, T. A. L.; Wang, Y. Coarse-Grained Force Field Calibration Based on Multiobjective Bayesian Optimization to Simulate Water Diffusion in Poly-*ε*-Caprolactone. *J. Phys. Chem. A* **2020**, *124*, 5042–5052.

(38) Rosasco, N. Valparaiso University Compute Systems. <https://www.valpo.edu/computing-information-sciences/faculty/nicholas-rosasco/compute-system-pascal-2/> (accessed 28 July, 2022).

(39) Park, J.-S. Optimal Latin-Hypercube Designs for Computer Experiments. *J. Stat Plan Inference* **1994**, *39*, 95–111.

(40) Wang, G. G. Adaptive Response Surface Method Using Inherited Latin Hypercube Design Points. *J. Mech. Des.* **2003**, *125*, 210–220.

(41) Fonseca, C. M.; Fleming, P. J. *Genetic Algorithms for Multi-objective Optimization: Formulation, Discussion and Generalization*, Proceedings of the Fifth International Conference on Genetic Algorithms, Morgan Kaufmann Pub Inc: San Mateo, 1993; pp 416–423.

(42) Ge, J.; Guo, L.; Wang, S.; Zhang, Y.; Cai, T.; Zhao, R. C. H.; Wu, Y. The Size of Mesenchymal Stem Cells Is a Significant Cause of Vascular Obstructions and Stroke. *Stem Cell Rev. Rep.* **2014**, *10*, 295–303.

(43) Binder, C.; Milleret, V.; Hall, H.; Eberli, D.; Lühmann, T. Influence of Micro and Submicro Poly(Lactic-Glycolic Acid) Fibers on Sensory Neural Cell Locomotion and Neurite Growth. *J. Biomed. Mater. Res.* **2013**, *101*, 1200–1208.

(44) de Ath, G.; Everson, R. M.; Rahat, A. A. M.; Fieldsend, J. E. Greed Is Good: Exploration and Exploitation Trade-Offs in Bayesian Optimisation. *ACM Trans. Evol. Learn. Optim.* **2021**, *1*, 1–22.